Nucl Eng Technol 47 (2015) 196–203

Available online at www.sciencedirect.com

ScienceDirect

journal homepage: http://www.journals.elsevier.com/nuclear-engineering-and-technology/

Original Article

MODE CONTROL OF GUIDED WAVE IN MAGNETIC HOLLOW CYLINDER USING ELECTROMAGNETIC ACOUSTIC TRANSDUCER ARRAY

AKINORI FURUSAWA, FUMIO KOJIMA[*]*, ATSUSHI MORIKAWA*

Department of Systems Science, Graduate School of System Informatics, Kobe University, 1-1 Rokkodai-cho, Nada-ku, Kobe-shi, Hyogo Prefecture 657-0013, Japan

ARTICLE INFO

Article history:
Received 10 October 2014
Received in revised form
8 December 2014
Accepted 10 December 2014
Available online 21 January 2015

Keywords:
Dispersion curve
Simulation
Structural Health Monitoring (SHM)
Ultrasonic

ABSTRACT

The aim of this work is to demonstrate a method for exciting and receiving torsional and longitudinal mode guided waves with an electromagnetic acoustic transducer (EMAT) ring array.

First of all, a three-dimensional guided wave simulator is developed in order to numerically analyze the propagation of the guided wave. The finite difference time domain method is used for the simulator. Second, two guided wave testing systems using an EMAT ring array are provided: one is for torsional mode (T-mode) guided wave and the other is for longitudinal mode (L-mode). The EMATs used in the both systems are the same in design.

A method to generate and receive the T- and L-mode guided waves with the same EMAT is proposed. Finally, experimental and numerical results are compared and discussed.

The results of experiments and simulation agree well, showing the potential of the EMAT ring array as a mode controllable guided wave transmitter and receiver.

1. Introduction

Guided wave is a kind of ultrasonic that is able to propagate over long distances along the longitudinal direction of the pipe or platelike structure. By virtue of this characteristic, ultrasonic guided wave is said to have a great potential for rapid, long-range, and safe nondestructive testing [1]. In recent years, as the number of aging nuclear power plants increases, guided wave testing has become more important.

Conventional guided wave testing systems are classified into two categories: those using piezoelectric transducers and those using magnetostrictive sensors [2,3]. It is well known that the use of piezoelectric transducers (PZT) is the conventional technique of guided wave testing. However, PZT requires a high-viscosity couplant. This is a disadvantage in industrial applications. Magnetostrictive sensors do not need a couplant and seem to be adequate for on-site use. However, they have less controllability because of the characteristic that their excitation power works uniformly in the circumferential direction. An electromagnetic acoustic transducer (EMAT) [4] is a transducer for noncontact ultrasonic excitation and reception, which does not require any couplant. Each EMAT can be actuated

* *Corresponding author.*
E-mail address: kojima@koala.kobe-u.ac.jp (F. Kojima).

http://dx.doi.org/10.1016/j.net.2014.12.007
1738-5733/Copyright © 2015, Published by Elsevier Korea LLC on behalf of Korean Nuclear Society.
Special Issue on ISOFIC/ISSNP2014.

individually to have the potential of multichannel operation as well as piezoelectric transducers. In addition, EMATs are simple, resistant to high-temperature environments [5], and economical. EMATs have many advantages compared to conventional transducers. Moreover, they could become a suitable driver for generating L-, T-, and F-mode guided waves. This offers advantages for on-site inspection and online monitoring of real plants. Therefore, EMATs have been tackled by researchers to apply it to guided wave testing systems [6].

In this paper, we demonstrate that EMATs arranged in the circumferential direction at regular intervals are able to excite and receive the L-mode guided wave and the T mode. First, the theoretical background for guided waves is provided. The dispersion curve of the group velocity is calculated, and our guided wave testing system is mathematically modeled. Then, a numerical algorithm for the model and an experimental setup of the guided wave testing system are introduced. Finally, simulation and experimental results are compared and discussed.

2. Theoretical background

2.1. *Dispersion curve and wave structure of guided wave in hollow cylinder*

Analytical investigation of the guided wave in a hollow cylinder dates back to the work of Gazis [7]. His work delivered a complete solution to harmonic guided wave modes propagating in an infinite hollow cylinder. According to Gazis [7], the dispersion curve and wave structure can be obtained from the characteristic (frequency) equation represented as follows with some modification regarding X_j:

$$c_{ij}X_j = 0 \quad (i,j = 1,\ldots,6), \tag{1}$$

where c_{ij} is a six-by-six matrix and X_j denotes the vector $X_j = \{A \;\; A_1 \;\; A_3 \;\; B \;\; B_1 \;\; B_3\}$. For details of the elements, refer to his work [7]. A solution of Equation 1 requires the determinant to equal zero, written as:

$$\det[c_{ij}] = 0 \quad (i,j = 1,\ldots,6). \tag{2}$$

Equation 2 is an implicit transcendental function of angular frequency ω and wave number k to be solved computationally. GNU Scientific Library [8] is used for the computation. Once values for ω and k satisfying Equation 2 are found, the dispersion curve can be plotted. Phase and group velocity are written as follows:

$$v_p = \omega/k, \tag{3}$$

$$v_g = d\omega/dk. \tag{4}$$

Wave structure, which indicates the relative amplitude of each component of the displacement field, is obtained by substituting the solution of Equation 1 X_j into Equations 10 and 12 in the work of Gazis [7]. An example of the dispersion curve and wave structure is shown in Fig. 1: the pipe medium is SS400, whereas its outer radius and inner radius are 60.5 mm and 49.5 mm, respectively.

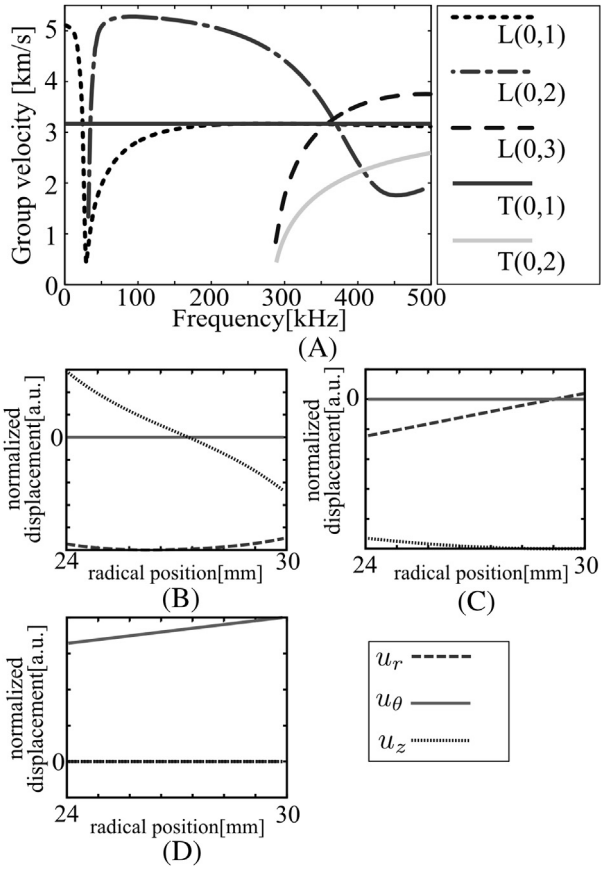

Fig. 1 – Example calculations. (A) Group velocity dispersion curve. Wave structures (B), (C), and (D) are L(0,1), L(0,2), and T(0,1) mode, respectively. The group velocity dispersion curve includes longitudinal and torsional modes. The representation of L(0,m) denotes the longitudinal mode of the *m*th degree in the radial direction. T(0,m) is the same as L(0,m).

2.2. *Guided wave propagating hollow cylinder*

Newton's equation of motion and Hooke's law in cylindrical coordinates are used for computation of the guided wave propagating in the pipe, as follows [9]:

$$\rho\frac{\partial}{\partial t}\dot{\mathbf{u}} = \begin{bmatrix} \frac{1}{r}+\frac{\partial}{\partial r} & -\frac{1}{r} & 0 & 0 & \frac{\partial}{\partial z} & \frac{1}{r}\frac{\partial}{\partial \theta} \\ 0 & \frac{1}{r}\frac{\partial}{\partial \theta} & 0 & \frac{\partial}{\partial z} & 0 & \frac{2}{r}+\frac{\partial}{\partial r} \\ 0 & 0 & \frac{\partial}{\partial z} & \frac{1}{r}\frac{\partial}{\partial \theta} & \frac{1}{r}+\frac{\partial}{\partial r} & 0 \end{bmatrix}\mathbf{T} + \mathbf{F}, \tag{5}$$

$$\frac{\partial}{\partial t}\mathbf{T} = [c]\begin{bmatrix} \frac{\partial}{\partial r} & \frac{1}{r} & 0 & 0 & \frac{\partial}{\partial z} & \frac{1}{r}\frac{\partial}{\partial \theta} \\ 0 & \frac{1}{r}\frac{\partial}{\partial \theta} & 0 & \frac{\partial}{\partial z} & 0 & \frac{\partial}{\partial r}-\frac{1}{r} \\ 0 & 0 & \frac{\partial}{\partial z} & \frac{1}{r}\frac{\partial}{\partial \theta} & \frac{\partial}{\partial r} & 0 \end{bmatrix}^{T}\dot{\mathbf{u}}, \tag{6}$$

where

$$\dot{\mathbf{u}} = [\dot{u}_r \quad \dot{u}_\theta \quad \dot{u}_z]^T, \tag{7}$$

$$\mathbf{T} = [T_{rr} \quad T_{\theta\theta} \quad T_{zz} \quad T_{\theta z} \quad T_{zr} \quad T_{r\theta}]^T, \tag{8}$$

$$\mathbf{F} = [F_r \quad F_\theta \quad F_z]^T, \tag{9}$$

where $\dot{\mathbf{u}}$, $\mathbf{T}$, $\mathbf{F}$, [c], and $\boldsymbol{\rho}$ are the particle velocity vector, stress vector, external force vector, stiffness tensor, and density, respectively. The free boundary condition is given as follows:

$$\begin{bmatrix} T_{rr} & T_{r\theta} & T_{rz} \\ T_{r\theta} & T_{\theta\theta} & T_{\theta z} \\ T_{zr} & T_{\theta z} & T_{zz} \end{bmatrix} \cdot \mathbf{n} = 0, \tag{10}$$

where $\mathbf{n}$ is the normal vector to each surface. The reference coordinates are shown in Fig. 2.

2.3. *Wave excitation force of EMAT*

In our previous work [10], we made the wave excitation mechanism of the typical type of EMAT clear in a computational manner. The wave excitation force of the EMAT consists of the Lorentz force, magnetization force, and magnetostriction. In case the EMAT is composed of a pair of magnets and a racetrack coil and set on the ferromagnetic plate, the Lorentz force and magnetization force cancel each other out to be almost zero. Eventually, the wave excitation force of the EMAT derives only from the magnetostriction along the tangential bias field. A schematic illustration of the basic principle and wave excitation force of the EMAT is shown in Fig. 3. On a ferromagnetic pipe, the wave excitation force of the EMAT is considered to act in a circumferential direction, the same as the case in the plate. Reception of the guided wave with EMAT is performed by the same mechanism of the excitation. To receive the guided wave, the EMAT receiver should be set in the same way as the EMAT transmitter is.

3. Guided wave testing simulator

3.1. *Finite difference time domain implementation*

We developed the guided wave simulator using the finite difference time domain (FDTD) method [9]. The reason why we chose the FDTD method is that it has many advantages compared to the finite element method (FEM): low computation cost, easy implementation, and compatibility with GPU enforcement. These advantages derive from the

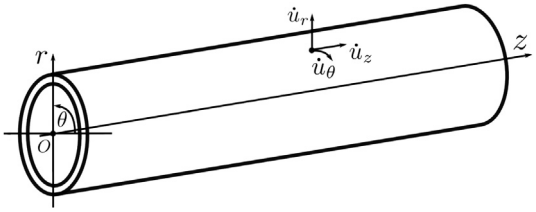

Fig. 2 – Reference coordinates.

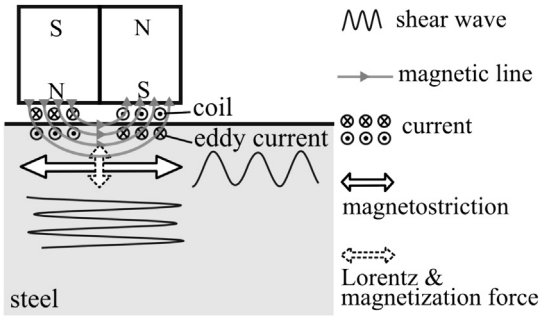

Fig. 3 – Basic principle of the electromagnetic acoustic transducer (EMAT) and the direction of the wave excitation force: magnetostriction, Lorentz force, and magnetization force. In this case, the Lorentz and magnetization force cancel each other out to be almost zero.

fact that the FDTD method is explicit, whereas the FEM is implicit. Hayashi and Rose [11] have proposed a semianalytical FEM to overcome the high computation cost of conventional FEM, but their method only applies to the axisymmetric case, and is impossible to apply to a pipe with arbitrarily shaped corrosion.

Fig. 4 illustrates the velocity–stress staggered-grid mesh used in the FDTD approach. The discrete forms of Equations 5 and 6 are given as follows

$$\dot{u}_{r_{i,j+\frac{1}{2},k+\frac{1}{2}}}^{n+1} = \dot{u}_{r_{i,j+\frac{1}{2},k+\frac{1}{2}}}^{n} + \frac{\Delta t}{\rho}\left[D_\theta T_{\theta\theta} + D_z T_{\theta z} + D_r T_{r\theta} + \frac{T_{r\theta}}{r}\right]_{i+\frac{1}{2},j,k+\frac{1}{2}}^{n+\frac{1}{2}}, \tag{11}$$

$$\dot{u}_{\theta_{i+\frac{1}{2},j,k+\frac{1}{2}}}^{n+1} = \dot{u}_{\theta_{i+\frac{1}{2},j,k+\frac{1}{2}}}^{n+1} + \frac{\Delta t}{\rho}\left[D_\theta T_{\theta\theta} + D_z T_{\theta z} + D_r T_{r\theta} + \frac{T_{r\theta}}{r}\right]_{i+\frac{1}{2},j,k+\frac{1}{2}}^{n+\frac{1}{2}}, \tag{12}$$

$$\dot{u}_{z_{i+\frac{1}{2},j+\frac{1}{2},k}}^{n+1} = \dot{u}_{z_{i+\frac{1}{2},j+\frac{1}{2},k}}^{n} + \frac{\Delta t}{\rho}\left[D_z T_{zz} + \frac{D_\theta T_{\theta z}}{r} + D_r T_{zr} + \frac{T_{zr}}{r}\right]_{i+\frac{1}{2},j+\frac{1}{2},k}^{n+\frac{1}{2}}, \tag{13}$$

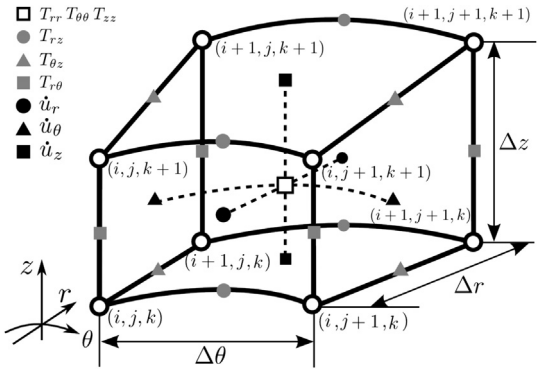

Fig. 4 – Variable arrangement of the velocity–stress staggered grid for the finite difference time domain (FDTD) method in cylindrical coordinates. The indices *i*, *j*, and *k* represent the values of spatial coordinates *r*, θ, and *z*, respectively.

$$T^{n+\frac{1}{2}}_{rr_{i+\frac{1}{2}j+\frac{1}{2}k+\frac{1}{2}}} = T^{n-\frac{1}{2}}_{rr_{i+\frac{1}{2}j+\frac{1}{2}k+\frac{1}{2}}} + \Delta t\left[c_{rr}D_r\dot{u}_r + \frac{c_{r\theta}}{r}(\dot{u}_r + D_\theta\dot{u}_\theta) + c_{r\theta}D_z\dot{u}_z\right]^n_{i+\frac{1}{2}j+\frac{1}{2}k+\frac{1}{2}}, \quad (14)$$

$$T^{n+\frac{1}{2}}_{\theta\theta_{i+\frac{1}{2}j+\frac{1}{2}k+\frac{1}{2}}} = T^{n-\frac{1}{2}}_{\theta\theta_{i+\frac{1}{2}j+\frac{1}{2}k+\frac{1}{2}}} + \Delta t\left[c_{r\theta}D_r\dot{u}_r + \frac{c_{rr}}{r}(\dot{u}_r + D_\theta\dot{u}_\theta) + c_{r\theta}D_z\dot{u}_z\right]^n_{i+\frac{1}{2}j+\frac{1}{2}k+\frac{1}{2}}, \quad (15)$$

$$T^{n+\frac{1}{2}}_{zz_{i+\frac{1}{2}j+\frac{1}{2}k+\frac{1}{2}}} = T^{n-\frac{1}{2}}_{zz_{i+\frac{1}{2}j+\frac{1}{2}k+\frac{1}{2}}} + \Delta t\left[c_{r\theta}D_r\dot{u}_r + \frac{c_{r\theta}}{r}(\dot{u}_r + D_\theta\dot{u}_\theta) + c_{rr}D_z\dot{u}_z\right]^n_{i+\frac{1}{2}j+\frac{1}{2}k+\frac{1}{2}}, \quad (16)$$

$$T^{n+\frac{1}{2}}_{\theta z_{i+\frac{1}{2}j,k}} = T^{n-\frac{1}{2}}_{\theta z_{i+\frac{1}{2}j,k}} + \Delta t\left[c_{\theta z}D_z\dot{u}_\theta + \frac{c_{\theta z}}{r}D_\theta\dot{u}_z\right]^n_{i+\frac{1}{2}j,k}, \quad (17)$$

$$T^{n+\frac{1}{2}}_{zr_{i,j+\frac{1}{2}k}} = T^{n-\frac{1}{2}}_{zr_{i,j+\frac{1}{2}k}} + \Delta t[c_{\theta z}D_z\dot{u}_r + c_{\theta z}D_r\dot{u}_z]^n_{i,j+\frac{1}{2}k}, \quad (18)$$

$$T^{n+\frac{1}{2}}_{r\theta_{i,j,k+\frac{1}{2}}} = T^{n-\frac{1}{2}}_{zr_{i,j,k+\frac{1}{2}}} + \Delta t\left[\frac{c_{\theta z}}{r}D_\theta\dot{u}_r + c_{\theta z}D_r\dot{u}_\theta\right]^n_{i,j,k+\frac{1}{2}}. \quad (19)$$

In these equations, the subscripts i, j, and k refer to the spatial indices, and the superscript n refers to the time index. Thus, the expression:

$$\dot{u}^{n+1}_{r_{i,j+\frac{1}{2}k+\frac{1}{2}}} \quad (20)$$

represents the r component of partial velocity evaluated at the point $r = i \times dr$, $\theta = [j + 1/2] \times d\theta$, $z = [k + 1/2] \times dz$, at the time $t = [n + 1] \times dt$. The symbols D_r, D_θ, and D_z denote the discrete form of the spatial differential operators: $\partial/\partial r$,$\partial/\partial\theta$, and $\partial/\partial z$. The specific expression of these operators is, for example, in the case of second-order approximation, given as follows:

$$D_rT_{rr}|_{i,j+\frac{1}{2},k+\frac{1}{2}} = \frac{1}{\Delta r}\left[T_{rr_{i+\frac{1}{2}j+\frac{1}{2}k+\frac{1}{2}}} - T_{rr_{i-\frac{1}{2}j+\frac{1}{2}k+\frac{1}{2}}}\right] \approx \frac{\partial T_{rr}}{\partial r}. \quad (21)$$

3.2. *Free boundary condition*

The free boundary condition is easily and adequately implemented by the introduction of the so-called zero-stress formulation [12]. Choosing the r axis as the vertical direction (positive up ward) and setting the free surface at $r = 0$, we must satisfy the following equation:

$$T_{rr} = T_{r\theta} = T_{zr} = 0|_{r=0}. \quad (22)$$

When Equation 22 is discretized, particular values of the particle velocity and stress components need to be specified at and above the free surface boundary in order to solve Equations [11–19]. Setting the free surface boundary at $ir = i$, as shown in Fig. 5, the values of the stress fields at and above the free boundary are obtained using the property of antisymmetry, written as follows:

$$T_{rr}|_{ir=i-1/2} = -T_{rr}|_{ii=i+1/2}, \quad (23)$$

$$T_{r\theta}|_{ir=i} = 0,\ T_{rz}|_{ir=i} = 0. \quad (24)$$

The free surface boundary is set to be coincident with the shear stress nodes for accurate computation [13]. Substituting Equations 23 and 24 to Equations 11, 18, and 19, we obtain the following:

$$\dot{u}^n_{r_{i,j+\frac{1}{2}k+\frac{1}{2}}} = \dot{u}^{n-1}_{r_{i,j+\frac{1}{2}k+\frac{1}{2}}} - \frac{2}{\Delta r}\times\frac{\Delta t}{\rho}\left[T^{n+\frac{1}{2}}_{rr_{i-\frac{1}{2}j+\frac{1}{2}k+\frac{1}{2}}}\right], \quad (25)$$

$$\dot{u}^n_{\theta_{i+\frac{1}{2}j,k+\frac{1}{2}}} = -\frac{2\Delta r}{2r-\Delta r}\frac{\dot{u}^n_{rj+\frac{1}{2}k+\frac{1}{2}} - \dot{u}^n_{r_{i,j-\frac{1}{2}k+\frac{1}{2}}}}{\Delta\theta} - \frac{(2r+\Delta r)}{(\Delta r-2r)}\dot{u}^n_{\theta_{i-\frac{1}{2}j,k+\frac{1}{2}}}, \quad (26)$$

$$\dot{u}^n_{z_{i+\frac{1}{2}j+\frac{1}{2}k}} = \dot{u}^n_{z_{i-\frac{1}{2}j+\frac{1}{2}k}} + \frac{\Delta r}{\Delta z}\left[\dot{u}^n_{r_{i,j+\frac{1}{2}k-\frac{1}{2}}} - \dot{u}^n_{r_{i,j+\frac{1}{2}k+\frac{1}{2}}}\right]. \quad (27)$$

Averaging Equations 26 and 27 with the corresponding inner values, we obtain the discrete forms of $\dot{u}_\theta$ and $\dot{u}_z$ on the free surface, written as follows:

$$\dot{u}^n_{\theta_{i,j,k+\frac{1}{2}}} = \frac{\dot{u}^n_{\theta_{i+\frac{1}{2}j,k+\frac{1}{2}}} + \dot{u}^n_{\theta_{i-\frac{1}{2}j,k+\frac{1}{2}}}}{2}, \quad (28)$$

$$\dot{u}^n_{z_{i,j+\frac{1}{2}k}} = \frac{\dot{u}^n_{z_{i+\frac{1}{2}j+\frac{1}{2}k}} + \dot{u}^n_{z_{i-\frac{1}{2}j+\frac{1}{2}k}}}{2}. \quad (29)$$

The free boundary conditions on the other planes are also obtained in the same manner.

4. Guided wave testing system using EMAT transmitter/receiver array

4.1. *System overview*

A schematic illustration of the guided wave testing system is shown in Fig. 6. The system is composed of a straight steel pipe (SS400), EMAT ring arrays for transmitter and receiver, a Japan Probe preamplifier (PR-60) for receiving EMAT, a Japan Probe pulse receiver (JPR-600C), and a personal computer for digital oscilloscope and band pass filter.

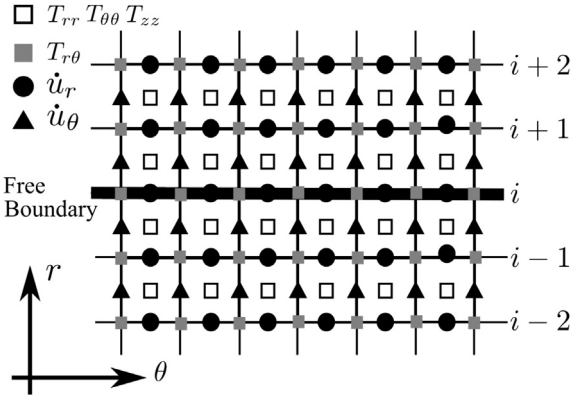

Fig. 5 – Free boundary and variables in an $r\ \theta$ plane. The bold unbroken line is a free boundary. Index i represents the spatial coordinate r.

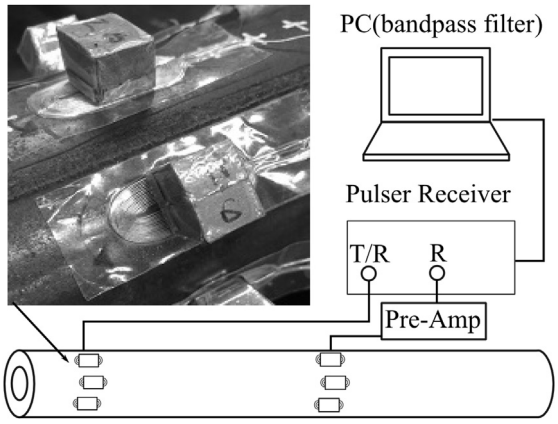

Fig. 6 – Schematic illustration of the guided wave system using an electromagnetic acoustic transducer (EMAT) ring array: a PC for digital oscilloscope and band pass filter, pulser/receiver, preamplifier, and EMAT ring array for the transmitter and receiver consisting of several EMATs.

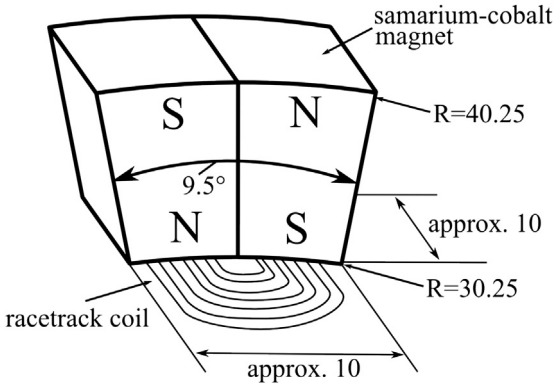

Fig. 7 – Configuration of the electromagnetic acoustic transducer (EMAT) used in the system.

Detailed specifications of the pulse receiver are listed in Table 1. The center frequency and gain of the preamplifier are 100 kHz and 60 dB, respectively.

The EMAT ring array for the transmitter and receiver is composed of eight EMATs. EMATs for the transmitter are series connected to be driven at the same time, whereas EMATs for the receiver are parallel connected in order to strengthen the signal intensity [14].

4.2. *Design of EMAT and layout for torsional/ longitudinal mode guided wave*

The design of the EMAT used in the system is illustrated in Fig. 7. The EMAT is composed of exchange coupled permanent magnets and a racetrack coil. Samarium–cobalt magnets are used in this work. The key parameters of the EMAT for the transmitter and the receiver are listed in Table 2. For excitation of the torsional mode guided wave, EMATs for the transmitter are set as shown in Fig. 8A to make the wave excitation force act in the circumferential direction. For the longitudinal mode guided wave, The EMATs are just set to rotate 90° around to make the excitation force act in the longitudinal direction, because these EMATs are mobile (see Fig. 8B).

EMATs for the receiver are set in the same manner as the transmitter. The reason is that the EMAT for the receiver is driven based on the same mechanism as the transmitter.

5. Results and discussion

5.1. *Simulation and experimental setup*

The experimental setup is illustrated in Fig. 9: an SS400 steel pipe with two EMAT ring arrays for transmitting and receiving. Each EMAT ring array has eight EMATs arranged in the circumferential direction at regular intervals. The key parameters in the simulation and experiment are listed in Table 3.

The wave excitation force for the torsional mode guided wave generated by the EMAT transmitter is assumed as follows in simulation:

$$\mathbf{F} = [W(t)\cdot\sin(2\pi f)0](0<t<5T_s), \tag{30}$$

where $W(t)$, f, and T_s denote a window function, frequency, and time, respectively. In this work, we use the $W(t)$ written as follows:

$$W(t) = \exp\left\{-\left(\frac{t-2.5\times10^{-6}}{1.75\times10^{-6}}\right)^2\right\}(0<t<5T_s). \tag{31}$$

The force for the longitudinal mode is written in the same way as the torsional mode,

$$\mathbf{F} = [0 \quad 0 \quad W(t)\cdot\sin(2\pi ft)](0<t<5T_s). \tag{32}$$

Simulator outputs are the circumferential components and longitudinal component of the particle velocity $\dot{u}_\theta$ and $\dot{u}_z$ at the receiving point, respectively. Simulations and experimental results are shown in Figs. 10A and 10B for the torsional mode guided wave and longitudinal mode guided wave, respectively. Fig. 10 shows that the real waveforms have virtually the same

Table 1 – Fundamental specifications of pulse receiver.

Pulser		Receiver	
Pulse type	Square burst	Frequency band width (Hz)	300 k–10M
Pulse voltage (V)	10–600	Gain (dB)	80
Number of waves	1–300	Input impedance (kΩ)	10
Transmitting frequency (Hz)	30 k–10M	Output impedance (Ω)	50

Table 2 – Parameters of coil used for EMAT.

		Transmitter EMAT	Receiver EMAT
Internal diameter (mm)	Major	21.0	18.0
	Minor	1.0	1.0
Wire thickness (mm)		0.26	0.18
Number of turns		15	30

EMAT, electromagnetic acoustic transducer.

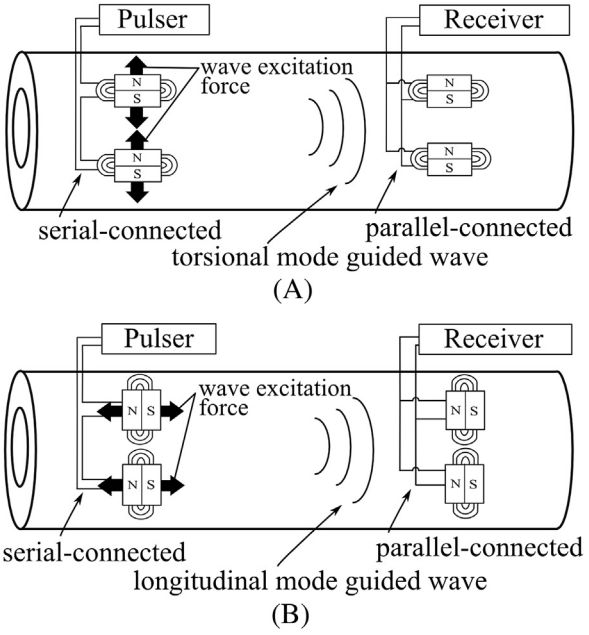

Fig. 8 – Layout methods. (A) Layout method for torsional mode guided wave excitation and reception. (B) Layout method for longitudinal mode guided wave excitation and reception using electromagnetic acoustic transducer (EMAT) ring arrays. EMATs for the transmitter are serial-connected and EMATs for the receiver are parallel-connected in order to enhance the signal intensity.

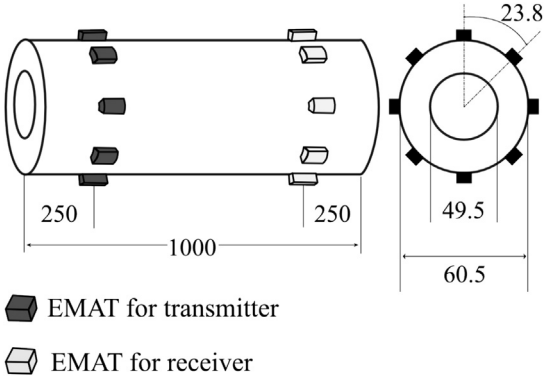

Fig. 9 – Simulation and experimental setup.

Table 3 – Parameters in simulation and experiments.

Simulation		Experiment	
Frequency (kHz)	100	Frequency (kHz)	100
dt (μs)	10	Voltage (V)	300
Young's modulus (GPa)	207	LPF (kHz)	70
Poisson ratio	0.3	HPF (kHz)	130
Density (kg/m^3)	7900	Gain (dB)	80
dr, dz (mm)	1	Wave cycles	5
dθ (rad)	0.0327	Pipe medium	SS400

HPF, high pass filter; LPF, low pass filter.

properties with the simulation for both the torsional and longitudinal waves.

5.2. *Analysis of the time of flight*

The group velocity of the torsional and longitudinal mode guided waves propagating in the pipe used in this experiment is shown in Fig. 1. First-order torsional mode [T(0,1)], first-order longitudinal mode [L(0,1)], and second-order longitudinal mode [L(0,2)] guided wave group velocity are 3166 m/s, 2822 m/s, and 5273 m/s, respectively. When the excitation frequency is 100 kHz, in the case of torsional mode, only T(0,1) mode is excited and in the case of longitudinal mode,

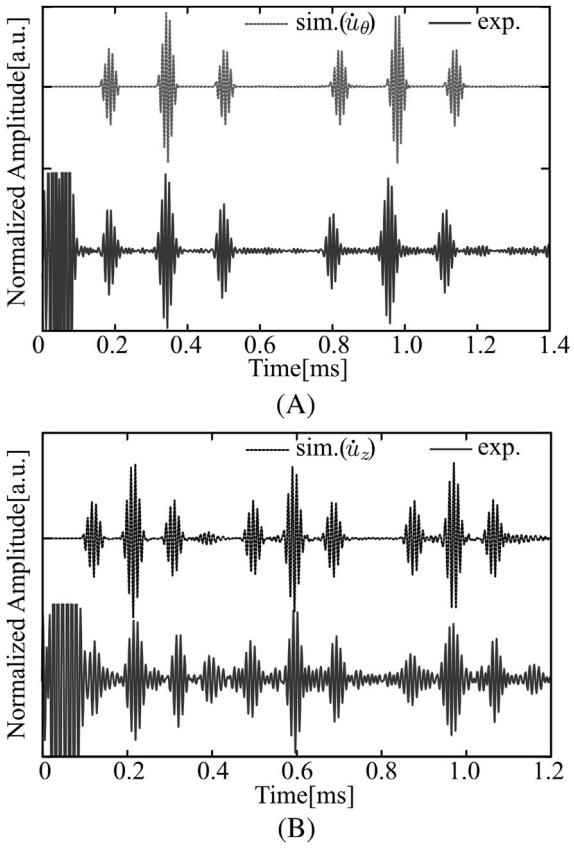

Fig. 10 – Comparison between simulation and experimental results. (A) Result of torsional mode guided wave excitation and reception. (B) Result of longitudinal mode guided wave. Red lines in A and B show experimental results, whereas green and blue lines show simulation results.

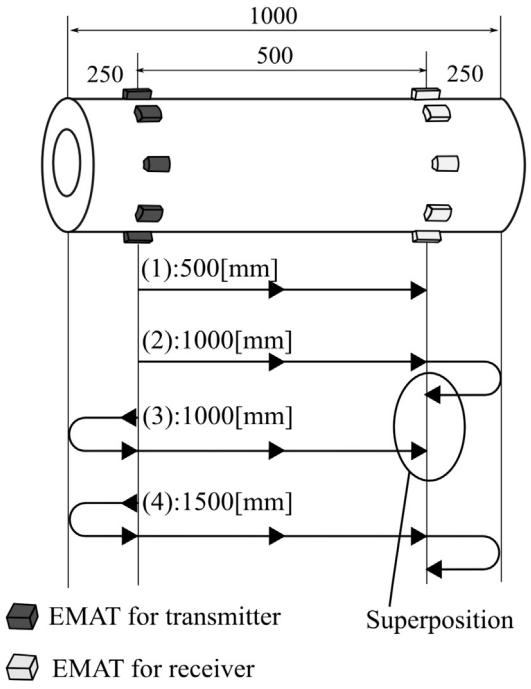

Fig. 11 – Schematic illustration of the propagation paths and the superposition that the guided waves reflected from left end and right end meet at.

L(0,1) and L(0,2) modes can be excited. The propagation paths of the wave bullets are illustrated in Fig. 11. The guided wave excited by the transmitter propagates in both directions and reflects at the pipe ends. Thus, the wave bullet coming at the receiver directly, the wave bullet reflected at the pipe end near the receiver, and the wave bullet reflected at the opposite pipe end are observed in this order.

In this experiment, the transmitter and the receiver are allocated at a specific position where the wave bullet reflected at the left end and right end reach at the same time. Therefore, the second wave bullet becomes lager than the others (see Fig. 10). Time-of-flight (TOF) values of the wave bullets in simulation, experiment, and the theoretical value that is calculated with analytical group velocity are listed in Table 4.

Table 4 – Comparison between TOFs and group velocities from simulations and experiments.

Torsional mode guided wave				
WB index	1	2	3	4
TOF (Sim.) (μs)	153.6	312.3	468.8	786.8
TOF (Exp.) (μs)	153.6	308.2	465.4	774.9
TOF (Theo. T(0,1))	157.9	315.8	473.7	789.6
Longitudinal mode guided wave				
WB index	1	2	3	4
TOF (Sim.) (μs)	90.0	185.2	289.8	355.2
TOF (Exp.) (μs)	–	184.6	288.4	368.0
TOF (Theo. L(0,1))	94.8	189.6	284.4	–
TOF (Theo. L(0.2))	–	–	–	354.3

TOF, time of flight; WB, Wave bullet.

The WB index in Table 4 represents the wave bullet index shown in Fig. 10 as the circled number. The TOFs of each wave bullet and the wave profiles are in good agreement.

Only the T(0,1) mode guided wave is excited in the torsional setup. L(0,1) and L(0,1) are mainly excited in the longitudinal setup. The cause of the slight error of TOFs and wave bullet velocity is considered to be in physical values (e.g., Young's modulus, Poisson ratio, and density). The real waveform of the longitudinal guided wave is relatively noisier than that of the torsional. A major reason is thought to be the receivers responding to other components of the mode affecting the wave profiles. Another reason is thought to be that unexpected modes are excited. Transmitters set at a regular interval in the circumferential direction could excite several modes [15].

5.3. *Summary and future works*

The velocity dispersion curve and wave structure of the typical guided wave mode were considered for guided wave propagation in a hollow cylinder. A guided wave propagation model was formulated in stress–velocity form and discretized using the FDTD method. A guided wave testing system using an EMAT ring array for transmitter and receiver was developed.

Simulation and experiments were performed for both the torsional mode (T mode) and the longitudinal mode (L mode). The experimental results were consistent with simulation in wave form profiles and TOFs. The T-mode guided wave is easily applied to nondestructive testing of the pipe because it is not dispersive at any excitation frequency and is less likely to damp. By contrast, the L-mode guided wave is dispersive depending on excitation frequency. However, it has the potential to be applied to advanced nondestructive testing method with sophisticated signal processing because of its dispersive characteristic. It is expected that the guided wave testing system we that have developed will lead to easy implementation of both T-mode and L-mode guided wave testing in the field. The feasibility of this guided wave system is under study.

Conflicts of interest

The authors declare no conflict of interests.

Acknowledgments

This work was partly supported by the JSPS Core to Core Program, A. Advanced Research Networks, "International research core on smart layered materials and structures for energy saving."

REFERENCES

[1] J.L. Rose, A baseline and vision of ultrasonic guided wave inspection potential, J. Pressure Vessel Technol. 124 (2002) 273–282.

[2] D.N. Alleyne, P. Cawley, The excitation of Lamb waves in pipes using dry-coupled piezoelectric transducers, J. Nondestruct. Eval. 15 (1996) 11–20.

[3] H. Kwun, K.A. Bartels, Magnetostrictive sensor technology and its applications, Ultrasonics 36 (1998) 171–178.
[4] R.B. Thompson, Physical Principles of Measurements with EMAT Transducers, Physical Acoustics, vol. XIX, Academic Press, New York, 1990, pp. 157–200.
[5] H. Nakamoto, F. Kojima, A. Morikawa, H. Tabata, D. Kosaka, Pipe-wall Thickness Measurement at High Temperature by Electromagnetic Acoustic Transducer, 18th International Workshop on Electromagnetic Nondestructive Evaluation (ENDE), Hotel Danube, Slovak Republic, Bratislava, June 2013.
[6] Y. Okawa, R. Murayama, H. Morooka, Y. Yamashita, Development of a movable inspection sensor for a pipe using an electromagnetic acoustic transducer of the magnetostriction effect type, Jpn. J. Appl. Phys. 48 (2009), 07GD07–07GD07-5.
[7] D.C. Gazis, Three-dimensional investigation of the propagation of waves in hollow circular cylinders: I. Analytical Foundation, J. Acoust. Soc. Am. 31 (1959) 568–573.
[8] [cited 2014 June], GNU Scientific Library Reference Manual, 2014. Available from: http://www.gnu.org/software/gsl/manual/.
[9] Y. Hao, M. Sato, FDTD formulation for analysis of elastic wave fields in cylindrical coordinates, J. Jpn. Soc. Simul. Technol. 20 (2001) 162–170.
[10] Fumio Kojima, Takafumi Ito, Numerical Simulation of Ultrasonic Source Mechanism for EMAT Based NDE System, Proceedings of the 19th Electromagnetic Nondestructive Evaluation (ENDE), Xi'an, China, June 25–28, 2014, pp. 42–43.
[11] T. Hayashi, J.L. Rose, Guided wave simulation and visualization by a semi-analytical finite element method, Mater. Eval. 61 (2003) 75–79.
[12] R.W. Graves, Simulating seismic wave propagation in 3D elastic media using staggered-grid finite differences, Bull. Seismol. Soc. Am. 86 (1996) 1091–1106.
[13] E. Gottschammer, K.B. Olsen, Accuracy of the explicit planar free-surface boundary condition implemented in a fourth-order staggered-grid velocity–stress finite-difference scheme, Bull. Seismol. Soc. Am. 91 (2001) 617–623.
[14] R. Murayama, K. Imai, N. Sonoda, Development of a Guided-wave Inspection System Using a Polarized Shear Wave and Evaluation of the Detective Performance of a Lot of Defects, 22nd MAGDA Conference, Miyazaki, Japan, Dec. 2013.
[15] M.J. Quarry, J.L. Rose, Multimode guided wave inspection of piping using comb transducers, Mater. Eval. 57 (1999) 1080–1090.